

**Modelling the permeability evolution of micro-cracked rocks from elastic wave velocity inversion
at elevated isostatic pressure**

Philip Benson^{1,2,3}, Alexandre Schubnel^{1,3}, Sergio Vinciguerra⁴, Concetta Trovato⁵, Philip Meredith² and
R. Paul Young³

¹Joint first authors

² Mineral, Ice and Rock Physics laboratory, University College London, Gower Street, London, WC1E
6BT, U.K.

³ Lassonde Institute, University of Toronto, 170 College street, Toronto, Ontario, M5S 3E3, Canada

⁴ Istituto Nazionale di Geofisica e Vulcanologia, Via di Vigna Murata 605, 00143, Rome, Italy

⁵ Dipartimento di Fisica e Astronomia, Università di Catania, Via di S. Sofia 64, 95123, Catania, Italy

ABSTRACT

A key consequence of the presence of microcracks within rock is their significant influence upon elastic anisotropy and transport properties. Here, two rock types (a basalt and a granite) with contrasting microstructures, dominated by microcracks, have been investigated using an advanced experimental arrangement capable of measuring porosity, P-wave velocity, S-wave velocity and permeability contemporaneously at effective pressures up to 100 MPa. Using the Kachanov (1994) non-interactive effective medium theory, the measured elastic wave velocities are inverted using a least square fit, permitting the recovery of the evolution of crack density and aspect ratio with increasing isostatic pressure. Overall, the agreement between measured and predicted velocities are good, with average error less than 0.05 km/s. At larger scales and above the percolation threshold, macroscopic fluid flow also depends on the crack density and aspect ratio. Using the permeability model of Guéguen and Dienes (1989) and the crack density and aspect ratio recovered from the elastic wave velocity inversion, we successfully predict the evolution of permeability with pressure for direct comparison with the laboratory measurements. We also calculate the evolution of the crack porosity with increasing isostatic pressure, based on the calculated crack density, and compare this directly with the experimentally measured porosity. These combined experimental and modelling results illustrate the importance of understanding the details of how rock microstructures change in response to an external stimulus when predicting the simultaneous evolution of rock physical properties.

1. INTRODUCTION

Under crustal conditions, cracks are ubiquitous on all scales in rocks. In the upper crust, the presence of cracks and fractures exerts a major influence on the physical and transport properties of rocks, despite the fact that cracks generally represent only small amounts of porosity (Walsh, 1965; Simmons et al., 1975). Isolated cracks make rocks more compliant, and connected cracks makes rocks more permeable. Where cracks are aligned, they can turn an initially isotropic rock into an anisotropic one. The superposition of different microcrack-forming mechanisms over extended periods of time may therefore give rise to a complex rock fabric, which in turn makes the task of interpreting field scale seismic surveys (for example) highly challenging, unless a-priory knowledge of the physical state of the rock is known and understood.

The existence of embedded microcracks helps to explain such observations as the difference between static and dynamic elastic moduli, and the elastic anisotropy present in rocks which do not exhibit any mineral preferred orientation (Kern, 1978). In seismotectonics, a still unanswered question is whether earthquakes and volcanic eruptions can be predicted, and time dependent elastic wave velocity variations have recently been considered as a possible precursory effect in certain cases (Chun et al., 2004; Gao and Crampin, 2004; Gerst and Savage, 2004). Similarly, the understanding and quantification of fluid flow through rocks is a key issue when considering the possible hydro-mechanical coupling taking place during the seismic cycle (Miller, 2002) or mechanisms leading to failure of volcano edifices such hydraulic fracturing, loss of block interlock, and hydrothermal weakening (Elsworth and Voight, 2001). It also has major implications when trying to forecast the life time of oil reservoirs or the integrity of underground hazardous waste storage. Fluid permeability has been analyzed in terms of percolation theory (Dienes, 1982; Madden, 1983; Rivier et al., 1985) and measured

experimentally for numerous rock types (Brace et al., 1968; Brace, 1980; Fischer and Paterson, 1992; Peach and Spiers, 1996; Benson, 2004; Benson et al., 2005).

Due to the difficulties of in-situ measurement of these parameters (e.g. permeability), a large number of diverse theoretical models have been presented that attempt to predict the change of one property of cracked rocks from the measurement of another property (e.g. O'Connell and Budiansky, 1974; Hudson, 1980; Nishizawa, 1982; Kachanov, 1994). However, in order to have confidence in the predictions of such models, we would ideally like to verify them by performing control experiments in which changes in all the relevant properties are measured on the same sample at the same time under the same conditions. Such an approach has the advantage that it eliminates potential errors caused by sample variability due to the natural heterogeneity and anisotropy of rocks. To date, such studies have been rare.

Here, we report experimental measurements of changes in porosity, P-wave velocity, S-wave velocity and fluid permeability made contemporaneously on rock cores under pressures simulating burial depths up to approximately 4 km (100 MPa). The results provide the required control in the form of a large, systematic dataset which is well suited for testing objectively models which aim to predict seismic velocity and permeability from microcrack fabric parameters. To our knowledge, the Kachanov (1994) non-interactive scheme is the simplest and most reliable method for the calculation of the full suite of crack density, aspect ratio and crack alignment parameters from elastic wave velocity data (Sayers and Kachanov 1995, Schubnel and Guéguen, 2003), and is employed in this study for these reasons. In addition, we have used the statistical percolation model of Guéguen & Dienes (1989) for estimating permeabilities. Because both models rely on the same crack parameters, their predictions can be compared to one another, and also to microstructural data.

2. EXPERIMENTAL EQUIPMENT AND METHODS

In order to study the key influence of microcrack alignment and anisotropy, we have chosen two volcanic rock types with strongly contrasting crack microstructures. Etnean basalt (EBD) is a porphyritic alkali basalt from Mount Etna, Italy, with an initial density of $2860 \pm 10 \text{ kg/m}^3$ and an initial porosity of 2.1% (Vinciguerra et al., 2005). This is an extrusive basalt which formed through the rapid cooling of lava flows. The rapid cooling has given rise to extensive fractures cutting the fine-grained glassy microstructure, with no apparent preferred microcrack alignment (Figure 1A, 1B). In contrast, Takidani granite (TDG) is a coarse-grained granodiorite from the Japanese Alps. It was collected from one of the youngest exposed plutons in the world at 1.2Ma (Kano and Tsuchiya, 2002). This material formed in an intrusive environment, where the relatively slow cooling rate resulted in a considerably lower crack density than that in the Etnean basalt. More importantly, however, the anisotropic stress field within the intrusion has produced an aligned microcrack fabric (Figure 1C, 1D) which, in turn, leads to anisotropy in the physical and transport properties (Benson, 2004). It is of note that the orientation of the aligned microcrack fabric is approximately co-linear with the larger (meter scale) joint fabric observed in outcrop (Kano and Tsuchiya, 2002; Benson, 2004). These microcrack fabrics were previously verified through 3-D elastic wave anisotropy measurements, in which TDG P-wave anisotropy of approximately 10% was measured, with a minimum principal direction aligned sub-normal to the microcracking plane (Benson, 2004; Benson et al., 2005). Similar elastic velocity measurements confirm the isotropic nature of Etnean basalt (Vinciguerra et al., 2005).

We have previously noted that, in order to eliminate potential errors caused by sample variability, we would ideally like to measure all the parameters of interest at the same time on the same sample under the same conditions. We have therefore developed an apparatus with the capability of

measuring contemporaneous changes in elastic wave velocities (P and S), porosity and permeability at elevated pressure (Jones & Meredith, 1998; Benson 2004; Benson et al., 2005).

The apparatus essentially comprises a 300 MPa isostatic pressure vessel equipped with dual servo-controlled 70 MPa pore fluid intensifiers. The intensifiers provide high pressure pore fluid (distilled water in this study) to each end of a test sample of 38.1 mm diameter and approximately 40 mm length, and are fitted with integral displacement transducers which enable them also to act as pore volumeters. Permeability measurements were made using the steady-state flow technique. A small but constant pressure difference is imposed across the sample and, once steady-state flow is established, permeability can be calculated from the flow rate via direct application of Darcy's law. For all the experiments reported here, the pressure difference across the sample was 0.5 MPa and the mean pore fluid pressure was 2.5 MPa. Although the apparatus is housed in a temperature-controlled laboratory, the internal vessel temperature is monitored continuously to ensure that measurement accuracy is not affected by temperature variations.

Permeabilities were calculated in real-time every 0.5 s using a rolling time window to calculate the fluid volume flow rate from the displacements of the two intensifiers. This procedure has the advantage of allowing the onset of steady-state flow to be quickly and easily defined, while also providing a real-time check against any leaks in the system (since the flow into the sample should be exactly equal and opposite to the flow out of the sample). From 100 sequential measurements of permeability during steady-state flow, we estimate the accuracy of our permeability measurements to be within approximately $\pm 5\%$. In addition, there will be an apparent change in permeability at elevated pressures due to the reduced dimensions (length and diameter) of the samples. We have measured the

changes in dimension, and analysis of the data shows that the maximum apparent change in permeability is less than 0.6% at the highest effective pressure (90 MPa). For the rocks measured in this study, permeability measurements were taken every 5 MPa at effective pressures from 5 MPa to 40 MPa, and every 10 MPa at effective pressures from 40 MPa to 90 MPa. In order to confirm that fluid flow was in the laminar regime where Darcy's Law is valid, we conducted experiments where the effective pressure was held constant but the pore fluid pressure gradient across the sample was varied. The different pressure gradients resulted in widely different volume flow rates, but the calculated permeabilities were the same within measurement accuracy (Benson,2004).

Measurements of the change in sample porosity with increasing effective pressure were made contemporaneously with the permeability measurements. Each step increase in effective pressure results in a decrease in internal pore volume and, hence, a tendency for pore fluid pressure to increase. However, the pore fluid pressure intensifiers are servo-controlled to maintain a constant pore fluid pressure. They therefore back-off to maintain the set pressure. Measurement of the piston displacements after re-equilibration therefore gives the pore volume change associated with the effective pressure increase. Comparison of the pore volume change with the initial porosity thus enables the porosity change to be calculated within an accuracy of approximately ± 0.01 percentage points for each effective pressure step.

Simultaneous elastic wave velocity measurements were made using the internal sample and measurement assembly illustrated in Figure 2. The assembly comprises two hollow, stainless steel endcaps that each house piezoelectric P-wave and S-wave transducers in a sealed, ambient pressure

cavity, and a pore fluid inlet or outlet port. The rubber jacketed rock sample is located between the two endcaps, and the whole assembly is held together by two stainless steel tie-bars.

3. MODELLING PHYSICAL PROPERTIES: KACHANOV (1994) AND GUÉGUEN AND DIENES (1989)

The effective physical (elastic and transport) properties of an initially isotropic cracked medium depend on a number of key parameters combining linear fracture mechanics and statistical physics. In the present method, we will use the following:

- Fluid bulk modulus (K_f) and matrix elastic properties (Young's modulus E_o and Poisson ratio ν_o)
- Crack geometry (in our case, we will consider penny shaped cracks - see Figure 3) with average aspect ratio defined by: $\zeta = \langle w/2c \rangle$.
- Crack density ρ , defined by: $\rho = \frac{1}{V} \sum_0^N c_i^3$, where c_i is the radius of the i^{th} crack, N being the total number of cracks embedded in the representative elementary volume V .
- Percolation factor f

3.1 ELASTIC PROPERTIES:

For an isotropic matrix containing a random distribution of cracks, the effective Young's modulus of a rock E^* is a linear function of the crack density which can be written in the form (first perturbation order):

$$\frac{E_o}{E^*} = 1 + H\rho \quad (1)$$

An exactly similar expression can be written for the effective shear modulus (μ^*). In equation 1, Young's modulus E_o is that of the crack-free matrix, and H is a positive scaling parameter which is dependent upon the matrix and fluid properties, the geometry of the cracks and the interactions between

them. The scalar H has been calculated by many authors for a wide variety of crack geometries and fluid properties. One of the most straightforward and least-controversial methods is Kachanov's (1994) non-interactive effective medium theory, which can be a valid approximation for low crack densities (up to ~ 0.5) (Kachanov, 1994; Schubnel and Guéguen, 2003). When neglecting crack interactions, effective elastic moduli of a cracked solid can be calculated *exactly and rigorously* in a unique manner that depends on the crack orientations and distribution solely. For certain distributions, where stress interactions are compensating geometrically such as a random (isotropic) or aligned crack distributions, it was shown that the non-interactive approximation is the most effective scheme when compared to other effective media theories (Kachanov, 1994; Sayers and Kachanov 1995). Moreover, in our case such a model is pertinent because cracks are elastically opening and closing due to isostatic pressure solely, whereas stress interactions are most important in the case of crack propagation only. In such a scheme, the evolution of elastic wave velocities can be used to quantify uniquely both the crack density and aspect ratios and thus forms the basis for the methods presented in this paper.

For a random distribution of crack centers and orientations, Kachanov (1994) showed that the effective Young's modulus E^* and shear modulus μ^* of a rock can be written as:

$$\frac{E_0}{E^*} = 1 + \left(1 + \frac{3}{5} \left[\left(1 - \frac{\nu_0}{2} \right) \frac{\delta}{1 + \delta} - 1 \right] \right) h\rho \quad (2)$$

and:

$$\frac{\mu_0}{\mu^*} = 1 + \left(1 + \frac{2}{5} \left[\left(1 - \frac{\nu_0}{2} \right) \frac{\delta}{1 + \delta} - 1 \right] \right) \frac{h\rho}{1 + \nu_0} \quad (3)$$

where the scalar $h = \frac{16(1-\nu_0^2)}{9(1-\nu_0/2)}$ is the appropriate one for a non-interactive penny shaped crack geometry (Kachanov, 1994; Sayers and Kachanov, 1995). The parameter δ is a non-dimensional number referred to as the saturation parameter, and is defined by $\delta = (1-\nu_0/2)h \frac{E_0 \zeta}{K_f}$. This co-efficient essentially compares the fluid bulk modulus K_f to the crack bulk modulus $E_0 \zeta$ (assuming that all change in the crack volume is due to aperture variations).

For a transversely isotropic distribution of microcracks, equations (2) and (3) were modified in terms of new effective elastic compliances (S^*) to take account of the inclusion of aligned cracks embedded within an uncracked rock matrix of compliance S^0 (as given by Sayers and Kachanov (1995) and Schubnel and Guéguen (2003)):

$$\begin{aligned}
S_{1111}^* &= S_{2222}^* = S_{1111}^0 + \frac{\rho}{E_0 h} \left(\langle n_1^2 \rangle + \left[\left(1 - \frac{\nu_0}{2}\right) \frac{\delta}{1 + \delta} - 1 \right] \langle n_1^4 \rangle \right) \\
S_{3333}^* &= S_{3333}^0 + \frac{\rho}{E_0 h} \left(\langle n_3^2 \rangle - \left[\left(1 + \frac{\nu_0}{2}\right) \frac{\delta}{1 + \delta} - 1 \right] \langle n_3^4 \rangle \right) \\
S_{1212}^* &= S_{1212}^0 + \frac{\rho}{E_0 h} \left(\frac{\langle n_1^2 \rangle}{2} + \left[\left(1 - \frac{\nu_0}{2}\right) \frac{\delta}{1 + \delta} - 1 \right] \frac{\langle n_1^4 \rangle}{3} \right) \\
S_{1313}^* &= S_{2323}^* = S_{1313}^0 + \frac{\rho}{E_0 h} \left(\frac{1 - \langle n_1^2 \rangle}{2} + \left[\left(1 - \frac{\nu_0}{2}\right) \frac{\delta}{1 + \delta} - 1 \right] \langle n_1^2 n_3^2 \rangle \right) \\
S_{1122}^* &= S_{1122}^0 + \frac{\rho}{E_0 h} \left(\left[\left(1 - \frac{\nu_0}{2}\right) \frac{\delta}{1 + \delta} - 1 \right] \frac{\langle n_1^4 \rangle}{3} \right) \\
S_{1133}^* &= S_{2233}^* = S_{1133}^0 + \frac{\rho}{E_0 h} \left(\left[\left(1 - \frac{\nu_0}{2}\right) \frac{\delta}{1 + \delta} - 1 \right] \langle n_1^2 n_3^2 \rangle \right)
\end{aligned} \tag{4}$$

Indices, 1, 2 and 3 refer to the principal axes given previously in Figure 3 where axis 3 is the axes of symmetry. n_i is the crack normal i^{th} component, and its average is defined for a distribution of crack orientations as:

$$\langle n_i \rangle = \frac{1}{2\pi} \int_0^{2\pi} d\phi \int_0^{\pi/2} F(\theta, \phi) n_i \sin\theta d\theta \quad (5)$$

with $F(\theta, \phi)$ being the orientation distribution function (cf. Figure 3). Note that the tensors $\langle n_i n_j \rangle$ and $\langle n_i n_j n_k n_l \rangle$ represent the second order and the fourth order moments of the crack orientation distribution function, respectively. Finally, note that the symmetry of the transversely isotropic distribution around axis 3 implies that $\langle n_i n_j \rangle = 0$ if $i \neq j$, $\langle n_i n_j^3 \rangle = 0$ if $i \neq j$, $\langle n_1^2 \rangle = \langle n_2^2 \rangle = (1 - \langle n_3^2 \rangle) / 2$, $\langle n_1^4 \rangle = \langle n_2^4 \rangle$ and $\langle n_1^4 \rangle = 3 \langle n_1^2 n_2^2 \rangle$ (Sayers and Kachanov, 1995; Schubnel and Guéguen, 2003).

These two forms of Kachanov's (1994) model (fully isotropic and transversely isotropic microcracks) provide suitable descriptions of the rocks measured in this study, since EBD has an approximately isotropic distribution of cracks, whereas the crack orientations within TDG exhibit approximate transverse isotropy. A better understanding of parameters such as crack aperture and aspect ratio will have direct application to modelling rock transport properties, such as permeability.

3.2 TRANSPORT PROPERTIES

For the rocks studied in this investigation, fluid flow is controlled by the linked network of microcracks. Understanding the key parameters describing the crack network geometry, such as crack density, size, aspect ratio and alignment, and their variation with applied pressure, is therefore essential in any attempt to predict permeability and its evolution with increasing effective pressure. Guéguen and Dienes (1989) showed that the permeability of microcracked rocks can be well represented by that of an

array of penny-shaped cracks embedded in an impermeable host matrix. Using the isotropic formulation of their percolation model, the bulk rock permeability k can be expressed as:

$$k = \frac{2}{15} f w^2 \zeta \rho \quad (6)$$

where, as earlier, ρ is the crack density, ζ and w the crack average aspect ratio and aperture respectively, and f is the percolation factor. The relation between f and crack density is shown in Figure 3. Percolation f can take any value between zero (all cracks are isolated and unconnected) and unity (all cracks are connected into the network). Guéguen et al., (1997) has shown that the percolation threshold (defined as the minimum crack density required in order to established a complete path for fluid to flow) for microscopic permeability is reached at a crack density of about 0.14, while the percolation threshold for macroscopic fracture is not reached until a crack density of approximately unity. For the crack densities encountered in the rocks studied here (ρ approximately 0.4 to 0.5 or less), the percolation factor f may be approximated by the connectivity factor f' (Guéguen and Dienes, 1989):

$$f' \approx \frac{9}{4} \left(\frac{\pi^2}{4} \rho - \frac{1}{3} \right)^2 \quad (7)$$

for $1/3 < \pi^2 \rho / 4 < 1$; the quantity ' $\pi^2 \rho / 4$ ' being the probability that two cracks intersect each other (Guéguen and Dienes, 1989).

4. ISOTROPIC CASE (ETNEAN BASALT): EXPERIMENTAL RESULTS AND INVERSION

For sake of simplicity, when modelling the elastic wave velocities for our two rock types, we restricted ourselves to the case of non-interacting microcracks saturated with water. For an isotropic distribution of cracks, the effective elastic properties predicted by Kachanov's (1994) model depend only upon the matrix Young's modulus and Poisson's ratio, the fluid compressibility and, importantly, the crack density and average aspect ratio.

Measurement of elastic wave velocities on Etnean basalt was made using three different cores taken from the same block of material. This serves two purposes. Firstly, to address any inhomogeneity issues present in the sample. Secondly, by drilling the cores with their long axis orthogonal to each other, it allows us to confirm the existence of an isotropically cracked rock fabric, as no significant velocity variation with coring direction (i.e. sample) was measured. This is also consistent with image analysis (Figure 1). Using equations (2) and (3), we performed a simple least square inversion of the laboratory-measured elastic wave velocities for crack density and aspect ratio at each stepwise increase in pressure. For the inversion, we used matrix (crack free) elastic parameters of $E_o = 100$ GPa and $\nu_o = 0.22$ calculated from the known rock composition, and for zero porosity. These elastic moduli equate to crack free elastic wave velocities equal to $V_p = 6.4$ km/s and $V_s = 3.75$ km/s. The fluid bulk modulus was taken as $K_f = 2$ GPa. Figure 4 shows the decrease in aspect ratio and crack density due to increasing effective pressure from the inversion of elastic wave velocity. As effective pressure is increased from 5 MPa to 80 MPa, crack density decreases from approximately 0.5 to approximately 0.3. Over the same pressure range, the crack aspect ratio decreases significantly, by one order of magnitude from 0.01 to 0.001. This result quantifies elastic crack closure and is entirely consistent with current theories (e.g. Hudson, 1980, 1990; Hudson et al., 1995; Sayers and Kachanov, 1995; Hudson et al., 2001). It is also

intuitively expected from the measured data, since both P-wave and S-wave elastic velocity increase with increasing effective pressure.

Figure 5 plots the forward solution of the crack density and aspect ratio to yield a calculated P and S elastic wave velocity (solid lines) for comparison with the laboratory data used as input for the inversions (symbols). Because there are no degrees of freedom in the inversion (we are fitting P and S wave velocities with crack density and aspect ratio as parameters), the agreement between laboratory data and the forward solution via the Kachanov (1994) model is excellent. In general, the average disagreement between measured and modeled velocities is less than 0.05 km/s. This exercise demonstrates the stability of the inversion (rather than the generation of new data per se).

Using the relation $\phi_c = N\pi c^2 w/V$ (where ϕ_c is the crack porosity, N is the total number of cracks, V the total volume of the rock, and w and c are the average crack radius and aperture respectively), and recalling the definition of crack density ρ and the aspect ratio ζ , we find a simple relationship linking ϕ_c to ρ and ζ as: $\phi_c = \pi\rho\zeta$. Using this expression, it is possible to calculate a crack porosity if we assume that all the porosity within the sample is composed of penny shaped cracks. This calculated crack porosity can then be compared directly with the experimentally measured porosity as a function of effective pressure, as shown in Figure 6. To allow for ease of comparison, the model porosity is set equal to the experimental porosity at a pressure of 5 MPa. Comparison between the change with increasing pressure of measured bulk porosity (symbols) and model porosity (solid and dashed lines), representing only crack porosity, is then straightforward. Experimentally measured bulk porosity decreases from approximately 2% to 1.4% as isostatic pressure is increased from 5 to 80 MPa. Comparison with the model (i.e. crack) porosity trend is good, suggesting that the porosity of Etnean

Basalt possesses a significant microcracked element. The process of setting model porosity equal to measured porosity allows us to evaluate the proportion of the total porosity that is quasi-equant or non-crack like, and therefore less compliant. For sample EBD-3 this is 0.9%; for EBD-6 it is 0.8%; and for EBD-9 it is 1.3%. Therefore an average of approximately 1% consists of quasi-equant or non-crack like porosity, which could be due to the formation of gas bubbles within the lava flow. Such void spaces resist increases in isostatic pressure very well, and are quasi-isotropic from the point of view of elastic wave velocity (Stanchits et al., 2005). In this way, they contribute to the bulk porosity; but not significantly to the variation of porosity and elastic wave velocity with pressure.

Recalling the results from the elastic wave velocity inversion (i.e. crack density and aspect ratio as a function of pressure), the only remaining unknown in equation 6 is the average crack aperture. Indeed, the connectivity factor itself is a function of the crack density. By assigning a suitable mean, constant, average aperture, it is now possible to predict the evolution of permeability. As for elastic wave velocity measurement previously, permeabilities were measured along the same three-orthogonal axes in order to assess the existence (or otherwise) of permeability anisotropy.

Figure 10A shows the experimentally measured values of permeability for EBD as a function of effective pressure (solid symbols), together with modeled values of permeability calculated using equations (6) and (7) and mean crack apertures of 0.8 μm (upper bound) and 0.5 μm (lower bound). As with the elastic wave velocity measurements, the use of three cores drilled orthogonal to each other confirms that the transport properties of this rock type are essentially isotropic. The bounds for the crack apertures are based on crack widths measured during SEM analysis of thin sections (e.g. Figure 1). Overall, the model permeabilities are in good agreement with the experimentally measured values,

although some scatter is evident. The comparison also suggests that the mean crack aperture decreases as effective pressure is increased, since the upper bound (0.8 μm) provides better agreement with the experimental data at low pressures, while the lower bound (0.5 μm) is in better agreement at the higher pressures.

5. TRANSVERSELY ISOTROPIC CASE (TAKIDANI GRANITE): EXPERIMENTAL RESULTS AND INVERSION

In the case of a transversely isotropic (TI) distribution of microcracks, the effective elastic compliance tensor S^* has five independent constants given by equation 4 and also depends on the mean orientation of the crack distribution with respect to the axis of symmetry (here, axis 3). As for the Etnean basalt samples, P-wave and S-wave velocity measurements for Takidani granite were measured along three orthogonal directions. In addition, since TDG is known to be anisotropic from 3-D velocity measurements (Kano and Tsuchiya, 2002; Benson, 2004, Benson et al., 2005), cores for measurement were taken along the three known principal anisotropy directions. Using this information as a guide and assuming a TI symmetry, four different independent elastic wave measurements were performed, i.e. P and S along the axis of symmetry (V_{33} and $V_{31}=V_{32}$ respectively) and P and S in the plane of isotropy ($V_{11}=V_{22}$, V_{12} respectively). As no diagonal measurements were realized, the model is under constrained. Indeed, one would need at least 5 independent wave velocity measurements just to successfully constrain the angle of the crack distribution and the crack density (Schubnel and Guéguen., [2003]), with further directional measurements needed to constrain the saturation. Despite these issues, the velocity data were inverted for crack density via equation (4) using a least squares technique, and using a constant crack aspect ratio of 0.001 estimated from image analysis of thin sections. Experimental evidence (Ayling et al., 1995) shows that this is likely to be a good assumption; as even though cracks close up with increasing pressure, disparities along the inner crack surfaces result in ‘pinch-outs’ that effectively keep the crack aspect ratio relatively constant over modest pressure changes (up to ~100 MPa). For the inversion, the matrix (crack free) elastic parameters were taken as $E_o = 80$ GPa and $\nu_o = 0.3$ (equivalent to elastic wave velocities of $V_p = 6.3$ km/s and $V_s = 3.35$ km/s). These crack-free parameters were estimated using the same method as described for EBD previously, and fluid bulk modulus was again taken as $K_f = 2$ GPa.

Figure 7 shows that, for TDG, the crack density decreases from 0.45 at 5 MPa effective pressure to 0.21 at 90 MPa. This compares with a crack density decrease from 0.50 to 0.35 for EBD over the same pressure range. Thus, the crack density in TDG exhibits a greater decrease over the same pressure range. This is likely to be due both to the lack of equant pores (gas bubbles) and the presence of lower aspect ratio cracks in TDG, which close more easily on the application of isostatic pressure. Calculations of crack porosity (ϕ_c), using the expression $\phi_c = \pi\rho\zeta$, as before, supports this interpretation. Indeed, figure 8 shows that the directly measured porosity (symbols) decrease with increasing effective pressure is much smaller (from 0.89% to 0.80%) than for EBD. The calculated crack porosity variation, using a constant aspect ratio of 0.001 (dashed line), exhibit a similar trend: from 0.885% to 0.815% over the pressure range 5 to 90 MPa, The overall agreement between both is good, but with a slightly smaller decrease at the higher pressures for the calculated porosity. This suggests that, in slight contrast to EBD, the porosity in TDG is strongly dominated by lower aspect ratio microcracks.

To test the stability and quality of the inversion, the crack density and aspect ratio data were again used to model the elastic wave velocity evolution by calculating the forward solution. The results are shown in Figure 9, together with the measured P-wave and S-wave velocities used as input. Like the EBD data, the experimentally measured elastic wave velocity increases markedly (~ 5.8 km/s to ~ 6.2 km/s for V_p) as effective pressure is increased. Unlike the EBD data, however, the velocities are anisotropic, and thus highly dependent upon measurement direction. In this case, the velocity measurements made approximately co-incident with the average microcrack symmetry plane (samples TDG-3 & TDG-14) are significantly higher than velocities made sub-normal to this plane (sample TDG-5). The fit between modeled and measured velocities is inferior compared to the Etnean basalt case,

despite the model taking TI into account. As stated above, this discrepancy is likely to be due to the fact that complete definition of TI symmetry requires five independent elastic constants, while only four independent elastic wave velocity measurements were performed. Despite this, the model data are within 2-3% of the measured data at 5 MPa and within about 1% at 90 MPa, and represent a good first-order solution to the problem. This error is close to the measurement accuracy of 1% and 2% for P-wave velocity and S-wave velocity, respectively.

When considering fluid flow, Takidani granite exhibits considerable permeability anisotropy, with permeability measured parallel to the microcracks three times higher than that normal to the microcracks (Figure 10B). In addition, this dependency of permeability anisotropy direction with crack fabric is the same as that with velocity anisotropy seen earlier. Strictly, anisotropic forms of the permeability equations (6 and 7) should be employed (e.g. Simpson et al., 2001). However, in our case the isotropic form of these expressions is a sufficient first approximation, as we have specifically taken cores in each of the principal anisotropy axes as determined from 3-D elastic wave velocity analysis noted earlier. The best model fit to the experimentally determined values of permeability are obtained with an upper crack aperture bound of 0.7 μm and a lower bound of 0.2 μm . A better fit could have been obtained by simply using equations 6 and 7 and the tensorial forms of the permeability and the crack density. In our case, unfortunately, this could not be performed as the full crack density tensor could not be recovered in the case of TDG due to lack of elastic wave data. However, even using the most simple isotropic case for permeability prediction, the trend of the permeability evolution with increasing isostatic pressure is well reproduced. In contrast to the permeability data for EBD, though, there is no strong evidence for the different aperture bound being better fits to the data at different pressures; as lower apertures are required at higher pressures, which is intuitively unphysical. Therefore, in the case

of TDG, the model provides no evidence of changing mean crack apertures with increasing isostatic pressure. However, as noted earlier, the situation is complicated by the fact that not only is there certainly a distribution of crack apertures (and aspect ratios), but also crack surface roughness as well. Increasing pressure will lead to perfect elastic crack closure only if there is no roughness. The existence of roughness may result in crack density, aspect ratio, and aperture variations less pronounced than otherwise. This rationale fits in well with the fact that the overall calculated decrease in permeability is higher than the observed permeability decrease.

6. DISCUSSION AND CONCLUSIONS

Etnean basalt is a typical lava flow basalt. It solidifies at temperatures of between about 500°C to 1200°C and pressures ranging from atmospheric to 3-4MPa (Rocchi et al., 2002). The rapid cooling associated with the deposition of this type of rock, together with the expulsion of volcanic gasses from the cooling magma, produces a highly fractured fabric, but with quasi-equant porosity likely resulting from gas pockets in the original lava flow. In general, these processes result in a relatively isotropic structure that is homogeneous on a mesoscopic scale. In contrast, Takidani granite formed over a relatively long time scale in an intrusive environment. The existence of major quaternary faulting, together with the WNW movement of the Pacific plate during the last 2 Ma, suggests that there exists a compressive tectonic stress field in the region aligned in a WNW to ESE orientation. It has been suggested that this stress field is responsible for the preferred alignment of both joint sets observed in outcrop, and the microcrack fabric (Kano and Tsuchiya, 2002). Previous work has shown that the microcrack fabric results in an anisotropy of approximately 10% in the P-wave velocity measured on laboratory samples, and that the principal anisotropy directions are essentially co-incident with the larger scale jointing (Kano and Tsuchiya, 2002; Benson, 2004).

As noted earlier, for both rock types a three orthogonal core-set was taken in order to confirm the existence or otherwise of anisotropy in each rock. In the case of TDG, the core set was taken co-incident to the known principal anisotropy axes. For Etnean basalt, the lack of variation in elastic wave velocity with sample orientation provides the confirmation of an isotropic crack fabric, also consistent with SEM observations. Application of isostatic pressure results in a 10% P-wave velocity increase from 5.5 to 6.0 km/s and a ten-fold decrease in permeability from 700 to $70 \times 10^{-18} \text{ m}^2$ as pressure is increased from 5 to 90 MPa. We have applied the models of Kachanov (1994) and Guéguen & Dienes (1989) to the laboratory data in order to interpret these observations in terms of the evolving microcrack fabric within the rock. Crack density decreases from 0.5 to 0.3, and aspect ratio decreases from 0.01 to 0.001 over the pressure increase 5 to 80 MPa, due to crack closure. Evidence of crack closure is also seen in the change in experimentally measured rock porosity, which decreases from 2% to 1.4% over the same pressure range. In contrast, the calculated model porosity decreases by an order of magnitude, from 1.0% to 0.1%, if porosity is assumed to be due solely to cracks. These observations are consistent with a highly cracked rock, with an embedded porosity of approximately 1% due to quasi-equant void spaces formed from gas bubbles in the lava flow. Equant voids are highly resistant to applied pressure, and are isotropic in terms of elastic wave velocities. Thus, they contribute significantly to the initial bulk porosity; but not to variations in permeability, elastic wave velocity or porosity as effective pressure is increased. The high bulk permeability and lack of any permeability anisotropy give additional support to this interpretation.

In contrast, both elastic wave velocity and permeability measurements show that the microstructural properties of Takidani granite are anisotropic. Elastic wave velocity measurements made approximately co-incident with the microcrack symmetry plane exhibit the highest P and S velocities,

whilst the lowest velocities were measured in sub-normal to this plane (Figure 9). This pattern is also seen in the permeability data. At 5 MPa, the initial permeability parallel to the microcracking plane (Figure 10), is in the range 20 to 30 x 10⁻¹⁸ m²; whereas normal to this plane it is approximately 8 x 10⁻¹⁸ m². Both elastic velocity and permeability exhibit marked changes as effective pressure is increased; with P-wave velocity increasing from about 5.8 to 6.2 km/s and permeability decreasing from about 20 to 0.8 x 10⁻¹⁸ m². Crack density evolution in TDG, calculated on the basis of the elastic wave velocities shows a decrease from 0.45 at 5 MPa, to approximately 0.20 at 90 MPa. The initial value is somewhat similar to that for EBD, but the change is much greater. This is entirely what would be expected for a rock microstructure containing cracks, but without any equant pores. To allow the TI implementation of the Kachanov model to be applied, the aspect ratio for this rock type (TDG) was fixed at 0.001. This value is primarily based upon the SEM observations, where 1000:1 cracks were commonly observed. Despite this being an ambient pressure measurement, this value is unlikely to change significantly (i.e. by an order of magnitude) upon the application of small amounts of isostatic pressure. This is demonstrated through the model of EBD aspect ratio change from 5 MPa to 10 MPa, which decreases by 21% (Figure 4). In addition, numerous authors have shown that once the aspect ratio is less than about 0.01, then any further decrease in aspect ratio make little difference to model output values (e.g. Bruner, 1976; Zimmerman, 1991).

In this study we calculate key rock microstructural parameters from elastic wave velocities (which are relatively easy to measure); and use them to guide inferences about other important rock physical properties, such as porosity and permeability, that we have also measured directly. The aim is to improve the ability of models, based on elastic wave velocity measurements, to predict parameters such as porosity and permeability at elevated pressure where they are difficult to measure. The first step in this process, reported here, has been progressively to quantify the link between elastic wave

velocities, key rock microstructural parameters such as crack density, aspect ratio and crack aperture, and transport properties such as permeability. The calculated porosity evolution derived from the crack density model for both EBD and TDG shows good fits to the decreasing porosity measured experimentally. This lends additional evidence that the void space in both rocks is composed primarily of microcracks. The comparison of this result to the permeability evolution with pressure further suggests that crack closure is the dominant mechanism for permeability reduction in these rocks.

Using the well constrained dataset, together with crack density derived from the Kachanov model and permeability calculated via Guéguen and Dienes model, a number of general conclusions may be drawn:

- I. Elastic wave velocity, velocity anisotropy, permeability, and permeability anisotropy are highly dependent upon effective pressure and the alignment of the overall microcrack fabric.
- II. Effective medium theory based on non interacting crack provides a solid framework with which to calculate rock properties, specifically in terms of the matrix elastic moduli, crack density, aspect ratio and alignment, pore fluid elastic moduli, and bulk porosity.
- III. For the two cracked rocks presented here, total crack densities cover the range 0.2 to 0.5. The solution for isotropic cracks as applied to Etnean basalt provides a more stable result than when modelling TI as applied to Takidani granite. Future TI inversions will incorporate more elastic wave velocity measurements in order to recover changing aspect ratio and improve accuracy.
- IV. The crack density and aspect ratio may be used to predict permeability under realistic in-situ conditions. A good match between calculated permeability and measured permeability is seen for values of crack aperture in the range 0.2 to 1.0 μm ; consistent with observation.

- V. For Etnean basalt a decrease in crack aperture is seen as isostatic pressure increases, whereas this is not seen in the Takidani granite. This is likely to be related to lower aspect ratio microcracks in TDG and thus to the formation of the rock.
- VI. Crack density is also related to porosity for these rock types. However, the bulk porosity is heavily influenced by processes (such as spherical voids in EBD) which do not effect elastic wave velocity evolution with pressure or direction.

7. ACKNOWLEDGEMENTS

This work was partially supported by a Canadian Natural Sciences and Engineering Research Council (NSERC) discovery grant to RPY, and partially by the UK Natural Environment Research Council (NERC); award NER/S/A/2001/06507 to PB. PB and PM would like to thank Catherine Stafford and Toru Takahashi (Fracture Research Institute, Tohoku University) for supplying the Takidani granite, and Erik Spangenberg (GeoForschungsZentrum, Potsdam) for aid in preparing the UV thin sections. AS would like to thank Jim Hazzard for aid in developing the Kachanov model code. The authors thank Yves Guéguen and an anonymous reviewer for helpful comments which greatly improved the manuscript.

8. REFERENCES

- Ayling, M.R., P.G. Meredith, and S.A.F. Murrell (1995), Microcracking during triaxial deformation of porous rocks monitored by changes in rock physical properties. 1. elastic-wave propagation measurements on dry rocks. *Tectonophysics*, 245, 205-221.
- Benson, P. M. (2004), Experimental study of void space, permeability and elastic anisotropy in crustal rock under ambient and isostatic pressure, Ph.D. thesis, 272pp., University of London, London.
- Benson, P. M., P. G. Meredith, E. S. Platzman, and R. E. White (2005), Pore fabric shape anisotropy in porous sandstone and its relation to elastic and permeability anisotropy under isostatic pressure, *Int. Journal. Rock. Mech.*, 42, 890-899, doi:10.1016/j.ijrmms.2005.05.003.
- Brace, W. F., J. B. Walsh, and W. T. Frangos (1968), Permeability of Granite under high pressure, *J. Geophys. Res.*, 73, 2225-2236.
- Brace, W. F. (1980), Permeability of crystalline and argillaceous rocks, *Int. J. Rock Mech. Min. Sci. Geomech. Abstr.*, 17, 241-251.
- Bruner, W. M. (1976), Comment on ‘Seismic velocities in dry and saturated cracked solids’ by R.J. O’Connell and B. Budiansky, *J. Geophys. Res.*, 81, 2573-2576.
- Chun, K.-Y., G. A. Henderson, and J. Liu (2004), Temporal changes in P wave attenuation in the Loma Prieta rupture zone, *J. Geophys. Res.*, 109, B02317, doi:10.1029/2003JB002498.
- Dienes, J. (1982), Permeability, Percolation and Statistical Cracks Mechanics, in *Issues in Rock Mechanics*, edited by R. E. Goodman and F. E. Heuze, pp. 86-94, American Institute of Mining, Metallurgical and Petroleum Engineers, New York.
- Elsworth, D., and B.Voight (2001). The mechanics of harmonic gas pressurisation and failure of lava domes. *Geophys. J. Intern.*, 145, 187-198.

- Fischer, G. J., and M. S. Paterson (1992), Measurement of Permeability and Storage Capacity in Rocks during Deformation at high Temperature and Pressure, in *Fault Mechanics and Transport Properties of Rocks*, edited by B. Evans and T-f Wong, pp. 213-252, Academic Press, San Diego.
- Gao, Y., and S. Crampin (2004). Observations of stress relaxation before earthquakes, *Geophys. J. Int.* 157, 578-582.
- Gerst, A., and M.K.Savage (2004). Seismic anisotropy beneath Ruapehu volcano: A possible eruption forecasting tool, *Science*, 306, 1543-1547.
- Guéguen, Y., and J. Dienes (1989), Transport properties of rocks from statistics and percolation, *Mathematical Geology*, 21, 1-13.
- Guéguen, Y., T. Chelidze, and M. Le Ravalec (1997), Microstructures, percolation thresholds, and rock physical properties, *Tectonophysics*, 279, 23-35.
- Hudson, J. A. (1980), Overall properties of a cracked solid, *Math. Proc. Camb. Phil. Soc.* 88, 371-384.
- Hudson, J. A. (1990), Overall elastic properties of isotropic materials with arbitrary distribution of circular cracks, *Geophys. J. Int.*, 102, 465-469.
- Hudson, J. A., E. Liu, and S. Crampin (1995), The mechanical properties of materials with interconnected cracks and pores, *Geophys. J. Int.* 124, 105-112.
- Hudson, J. A., T. Pointer, and E. Liu (2001), Effective-medium theories for fluid-saturated materials with aligned cracks, *Geophys. Prosp.*, 49, 509-522.
- Jones, C., and P. Meredith (1998), An experimental study of elastic wave propagation anisotropy and permeability anisotropy in an illitic shale. Presented at Eurock 98, Proc. SPE/ISRM Rock Mechanics in Petroleum Engineering, vol.1, 307-314, Trondheim, Norway.
- Kano, S., and N. Tsuchiya (2002), Parallelepiped cooling joint and anisotropy of P-wave velocity in the Takidani granitoid, Japan Alps. *J. Volcanology and Geothermal Res.*, 114, 465-477.

- Kachanov, M. (1994), Elastic solids with many cracks and related problems, *Adv. Appl. Mech.*, 30, 259-445.
- Kern, H. (1978), The effect of high temperature and high confining pressure on compressional wave velocities in quartz bearing and quartz free igneous and metamorphic rocks, *Tectonophysics*, 44, 185-203.
- Madden, T. R. (1983), Microcrack connectivity in rocks: a renormalization group approach to the critical phenomena of conduction and failure in crystalline rocks, *J. Geophys Res.*, 88, 585-592.
- Miller, S. A. (2002), Properties of large ruptures and the dynamical influence of fluids on earthquakes and faulting, *J. Geophys. Res.*, 107(B9), 2182, doi:10.1029/2000JB000032.
- Nishizawa, O. (1982), Seismic velocity anisotropy in a medium containing oriented cracks: Transverse isotropy case, *J. Phys. Earth*, 30, 331-347.
- O'Connell, R. and B. Budiansky (1974), Seismic velocities in dry and saturated rocks, *J. Geophys. Res.*, 79, 5412-5426.
- Peach, C. and C. Spiers (1996), Influence of crystal plastic deformation on dilatancy and permeability development in synthetic salt rock, *Tectonophysics*, 256, 101-128.
- Rivier, N., E. Guyon, and E. Charlaix (1985), A geometrical approach to percolation through random fractured rocks, *Geological Magazine*, 122, 157-162.
- Rocchi, V., P.R. Sammonds and C.R.J. Kilburn (2002), Flow and fracture maps for basaltic rock deformation at high temperatures, *J. Volc. Geotherm. Res.*, 120, 25-42.
- Sayers, C. M. and M. Kachanov (1995), Microcrack induced elastic wave anisotropy of brittle rocks, *J. Geophys. Res.*, 100, 4149-4156.
- Schubnel, A. and Y. Guéguen (2003), Dispersion and anisotropy in cracked rocks, *J. Geophys. Res.*, 108, 2101, doi:10.1029/2002JB001824.

- Simmons, G., T. Todd, and W. S. Balridge (1975), Toward a quantitative relationship between elastic properties and cracks in low porosity rocks, *Am. J. Sci.*, 275, 318-345.
- Simpson, G., Y. Guéguen, and F. Schneider (2001), Permeability enhancement due to microcrack dilatancy in the damage regime, *J. Geophys. Res.*, 106, 3999-4016.
- Stanchits, S., S.Vinciguerra and G. Dresen (2005), Ultrasonic velocities, acoustic emission characteristics and crack damage of basalt and granite, *Pure Applied Geophysics*, In Press.
- Vinciguerra, S., C. Trovato, P. Meredith, and P. Benson (2005), Relating seismic velocities, thermal cracking and permeability in Mt. Etna and Iceland basalts. *Int. Journal. Rock. Mech.*, 42, 900-910, doi:10.1016/j.ijrmms.2005.05.022.
- Walsh, J. B. (1965), The Effect of Cracks on the Compressibility of Rock, *J. Geophys. Res.*, 70, 381-389.
- Zimmerman, R.W. (1991), *Compressibility of Sandstones*, 173 pp., Developments in Geoscience, no.29., Elsevier, New York.

Figure Captions

Figure 1. (A): Etnean Basalt matrix detail using scanning electron microscopy (SEM: polished thin section) showing essentially randomly orientated microcracks. (B): thin section of the same rock type, with microcracking highlighted through impregnation of a UV-fluorescent dye. In contrast, Takidani granite exhibits an aligned crack fabric, as illustrated by an SEM image of a freshly broken rock surface (C) and, (D) UV dye impregnated thin section.

Figure 2. Schematic of sample and end-cap arrangement within the 300MPa isostatic pressure vessel showing key components. Sample size is 38.1mm diameter by approximately 40 length.

Figure 3. (Left) the penny-shaped crack geometry used in this study, and (right) the theoretical evolution of percolation (f), as compared to the approximation introduced by Guéguen & Dienes (1989), termed connectivity f^* , as a function of crack density.

Figure 4. Decrease of (left) crack density and (right) aspect ratio as a function of increasing effective confining pressure for Etnean Basalt. Note that the three samples measured (EBD -3, -6 and -9) were intentionally taken at right angles to each other to test for anisotropy in this rock type.

Figure 5. Forward solution (i.e. velocity) of Etnean basalt derived from the model crack density and aspect ratio (solid lines); with experimentally measured values shown as symbols (solid symbols denote V_p data; open symbols, V_s). For both P-wave velocity (upper plot) and S-wave velocity (lower plot) the discrepancy between the forward solution and laboratory velocities is less than approximately 0.05 km/s.

The use of three samples cored orthogonally to each other again demonstrates the isotropic nature of this material, especially at pressures above ~40 MPa.

Figure 6. Calculated porosity variation (lines) compared to measured porosity (symbols) for Etnean basalt as a function of effective pressure.

Figure 7. Decrease of model crack density as a function of effective pressure for Takidani granite. Note that as the transverse isotropy model requires cores in three orthogonal directions (as presented in this study), the model crack density is a least square fit to the total input data, hence the single trend even though three input cores were used.

Figure 8. Calculated porosity variation (dashed lines) compared to measured porosity decrease (symbols) as a function of effective pressure for Takidani granite. Error is approximately $\pm 0.01\%$ points. Note that, in a similar fashion to Figure 7, only a single trend is output (average) due to the nature of the TI model.

Figure 9. Forward solution of Takidani granite derived from the model crack density and aspect ratio (solid lines); with experimentally measured values shown as symbols. The use of three samples cored orthogonally to each other demonstrates the anisotropic nature of this material, with the slowest velocities measured sub-normal to the visible microcracking (sample TDG-5). Indices refer to the general co-ordinate frame given in Figure 3, with the first index referring to wave direction, and the second index referring to wave motion direction: $V_{11}(=V_{22})$ is equivalent to V_p measurement orthogonal to the crack plane (as defined by plane 1-2 in Figure 3, and measured in previous work, e.g. Benson,

2004); V_{33} is equivalent to V_p measurements made along axis '3' or normal to the crack plane; V_{21} ($=V_{12}$) is equivalent to V_s measurement in the crack plane with S-wave polarization also in that plane (i.e. S_h); and V_{23} ($=V_{31}$) is equivalent to V_s measurement made orthogonal to the crack plane with S-wave polarization along the '3' and '1' axes respectively (i.e. S_h).

Figure 10. Permeability variation with isostatic pressure for (A) Etnean basalt, and (B) Takidani granite. Symbols denote experimental measurements, and lines denote model permeability variation of constant crack aperture. Note that Etnean basalt shows essentially no permeability anisotropy, whilst for Takidani granite, sample TDG-5 exhibits a far lower permeability at all pressures than either TDG-3 or TDG-14. Experimental error in permeability is approximately $\pm 5\%$, thus, permeability change at high effective pressures (over $\approx 70\text{MPa}$) is essentially zero.

Figure 1

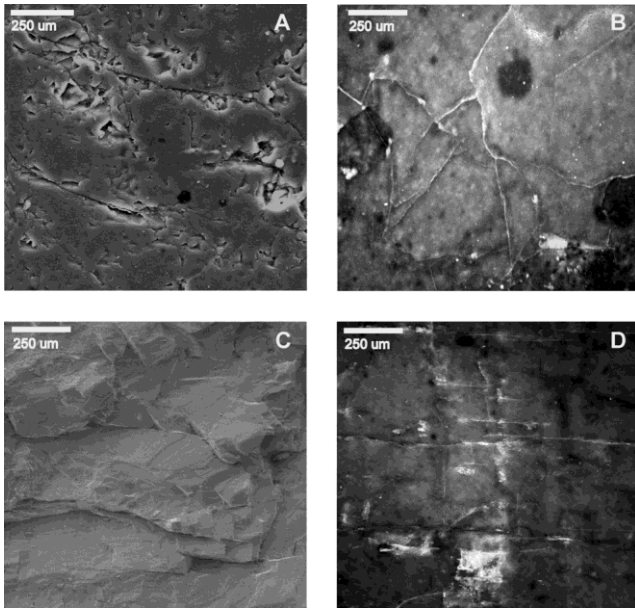


Figure 2

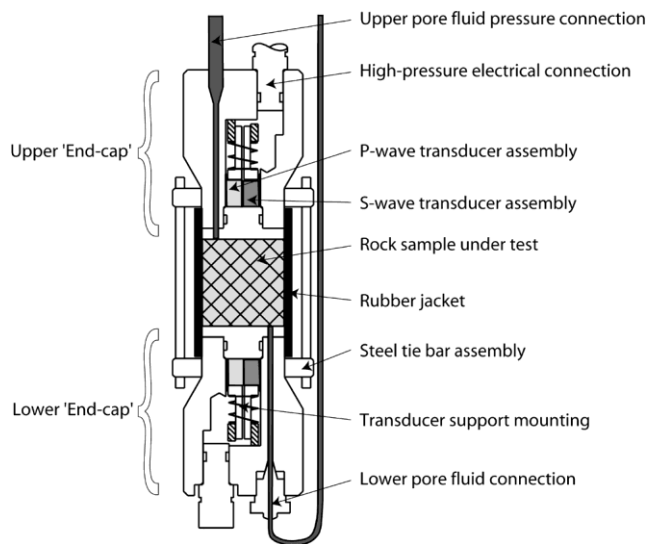


Figure 3

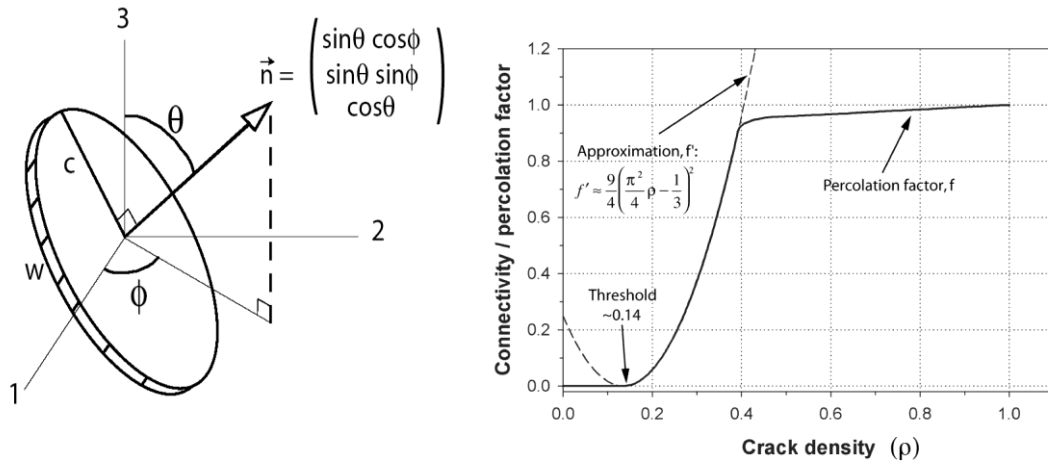


Figure 4

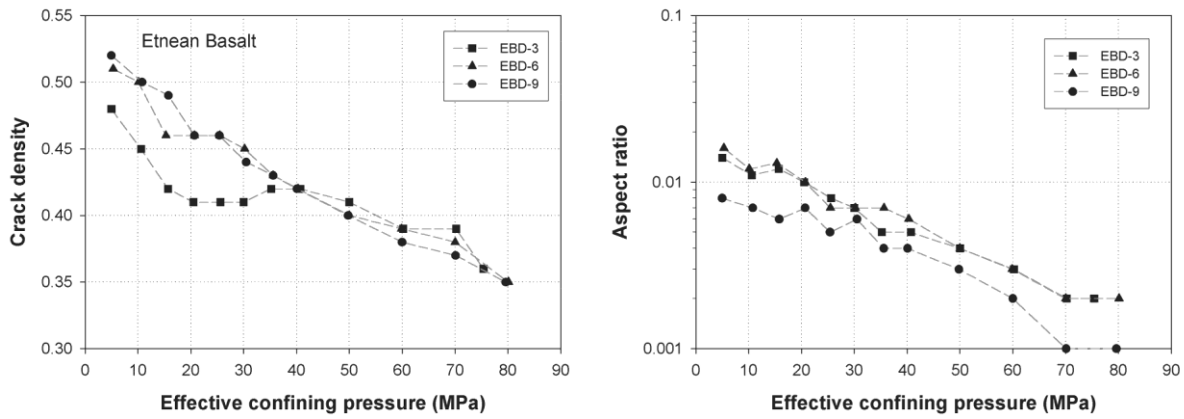


Figure 5

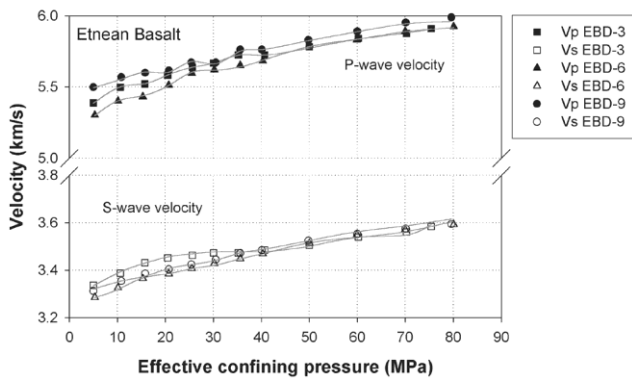


Figure 6

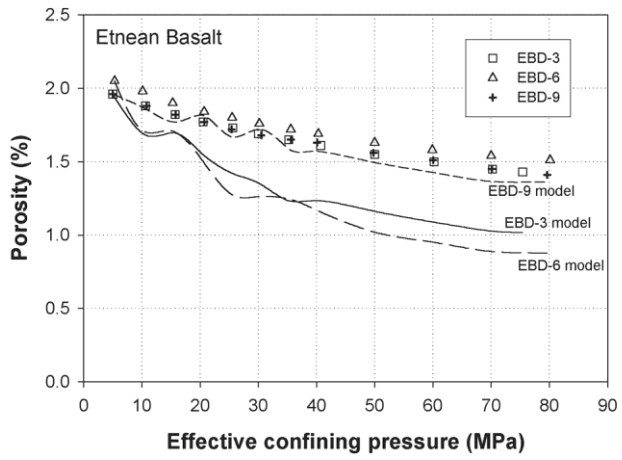


Figure 7

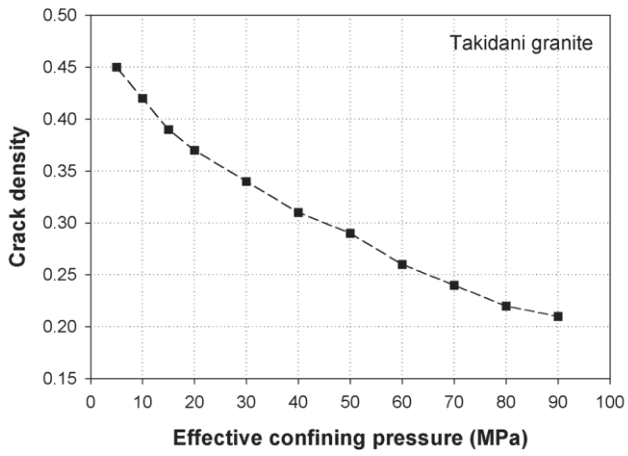


Figure 8

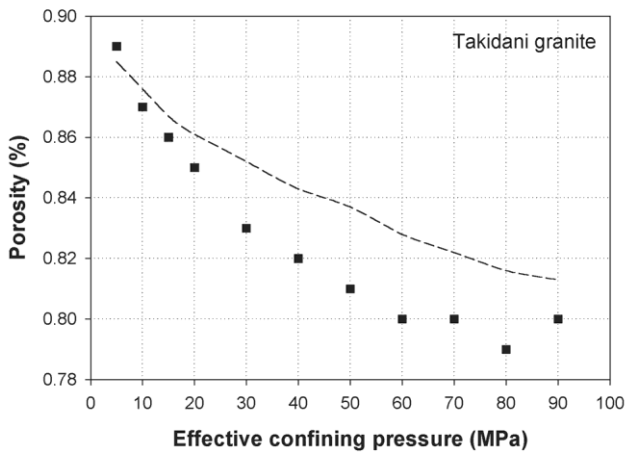


Figure 9

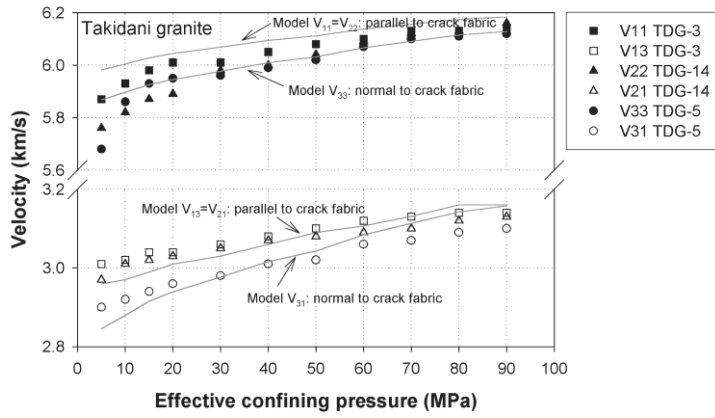


Figure 10

